Photonic band-gap waveguide microcavities: Monorails and air bridges

Kuo-Yi Lim,[a] D. J. Ripin, G. S. Petrich, L. A. Kolodziejski, E. P. Ippen, M. Mondol, and Henry I. Smith
Department of Electrical Engineering and Computer Science, Massachusetts Institute of Technology, Cambridge, Massachusetts 02139

P. R. Villeneuve, S. Fan, and J. D. Joannopoulos
Department of Physics, Massachusetts Institute of Technology, Cambridge, Massachusetts 02139

Photonic band-gap monorail and air-bridge waveguide microcavities, operating at the wavelength regime of 1550 nm, are fabricated using GaAs-based compound semiconductors. The fabrication process involves gas-source molecular beam epitaxy, electron-beam lithography, reactive ion etching, and thermal wet oxidation of $Al_{0.93}Ga_{0.07}As$. The fabrication of the air-bridge microcavity, in particular, also entails the sacrificial wet etch of Al_xO_y to suspend the micromechanical structure. The monorail and air-bridge microcavities have been optically characterized and the transmission spectra exhibit resonances in the 1550 nm wavelength regime. Tunability of the resonant wavelength is demonstrated through changing the defect size in the one-dimensional photonic crystal. The quality factors (Q) of the microcavities are about 140 for the monorail and 230 for the air bridge, respectively. © *1999 American Vacuum Society.* [S0734-211X(99)03303-X]

I. INTRODUCTION

The ability to control spontaneous emission promises reduced lasing thresholds and higher modulation speeds of semiconductor lasers, as well as increased light output and narrowed output linewidth in light-emitting devices. When an atom is placed in a microcavity, the spontaneous emission rate of that atom into a particular electromagnetic mode is enhanced over that in free space[1,2] by the factor η, where

$$\eta = \frac{Q}{4\pi V}\left(\frac{\lambda}{n}\right)^3.$$

In the expression, the cavity factor Q is defined as the number of optical oscillations for the electromagnetic energy of the resonant mode to decay to $e^{-2\pi}$ of its initial value, and provides a measure of the loss in the microcavity. Also, the modal volume is denoted as V, the free-space wavelength as λ, and the refractive index of the cavity material as n. A microcavity with a small resonant modal volume and a high cavity quality factor will thus result in a strong enhancement of spontaneous emission.

The photonic crystal[3,4] presents an attractive approach to realizing microcavities with high Q and small V. A photonic crystal is the photonic analogue of an electronic crystal. A photonic band structure describes the solutions to Maxwell's equations for a periodic lattice of dielectric material. Analogous to the electronic crystal, a photonic band gap (PBG) opens up at the Brillouin zone edges and defines a range of photon energies (or frequencies) where no electromagnetic propagation is allowed. The introduction of a defect in the photonic crystal breaks the periodicity and introduces a defect state within the PBG. Light is strongly confined around the defect region and a microcavity can thus be effectively formed.

A simple microcavity can be realized by implementing a one-dimensional photonic crystal for confinement in one direction and employing index confinement in the remaining two directions. The resulting waveguide microcavity structure has a very small modal volume, and also presents the opportunity to characterize the microcavity via use of coupling waveguides to couple light into and out of the microcavity. The largest cavity quality factor is achieved by surrounding the microcavity in air for maximum index contrast.

This article describes the fabrication and operation of one-dimensional photonic band-gap waveguide microcavities at $\lambda = 1550$ nm using GaAs-based compound semiconductors. Light is confined along the waveguide axis by a one-dimensional photonic crystal and in the other two directions by index guiding. The photonic crystal is defined by a periodic array of holes in the waveguide, with a cavity or defect region created by increasing the distance between two holes in the middle of the array. Fabrication techniques such as gas-source molecular beam epitaxy, direct-write electron-beam lithography, reactive ion etching, and wet thermal oxidation of $Al_xGa_{1-x}As$ are employed. The transmission characteristics of the microcavities are optically measured and the first operation of an air-bridge microcavity (initially proposed in Ref. 5) is reported. The passive waveguide microcavities described here are the first step toward realizing active microcavities and the control of spontaneous emission.

II. EXPERIMENTAL APPROACH

A. Device description

The photonic band-gap microcavities are manifested in two configurations, namely, the monorail [Fig. 1(a)] and the air-bridge [Fig. 1(b)] structures. The GaAs waveguide microcavity is either supported on a low refractive-index Al_xO_y material (the monorail) or suspended in air (the air bridge).

[a]Corresponding author; electronic mail: limky@mit.edu
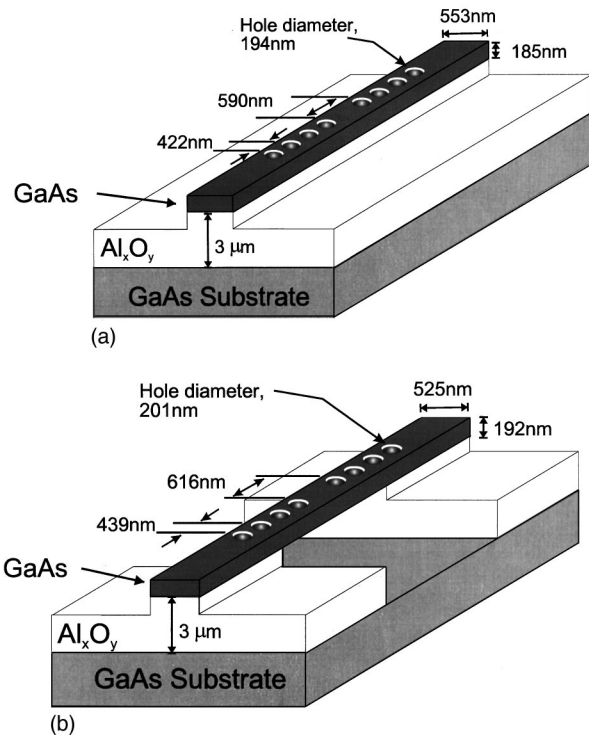
(a)

(b)

FIG. 1. Schematics of the photonic band-gap waveguide microcavities. The GaAs waveguide microcavity is either (a) supported on a low refractive-index Al_xO_y material (the monorail) or (b) suspended in air (the air bridge). The one-dimensional photonic crystal is defined by a periodic array of eight holes; a defect region is created in the crystal by increasing the distance between two holes in the middle of the array.

The air-bridge microcavity is expected to exhibit a higher cavity quality factor Q than the monorail microcavity, due to the larger index contrast between the waveguide microcavity and its surroundings. Increasing the number of holes in the photonic crystal also increases the Q for both microcavity structures, although the value of Q saturates with the increasing number of holes. This is due to an increased loss of light through coupling into free-space radiation modes. Widening the defect region in both microcavity structures has the effect of increasing the resonant wavelengths of the microcavities. In addition, altering the dimensions of other features in the microcavity structure also affects the positions of the band edges and the resonant wavelengths in the transmission spectra. For instance, a slight increase in the thickness of the waveguide has the primary effect of shifting the band edges to longer wavelength. A detailed theoretical treatment of the PBG waveguide microcavities can be found in Refs. 5 and 6.

For the monorail microcavity, the waveguide is 553 nm wide and 185 nm thick. The holes are 194 nm in diameter and are placed 422 nm apart (measured from center to center of the holes), while the defect width ranges from 561 to 708 nm (center to center of holes neighboring the defect region). For the air-bridge microcavity, the waveguide is 525 nm wide and 192 nm thick, the holes are 201 nm in diameter and laced 439 nm apart, while the defect width ranges from 585 to 738 nm. These physical dimensions are chosen to optimize the transmission at the resonant wavelength in the re-
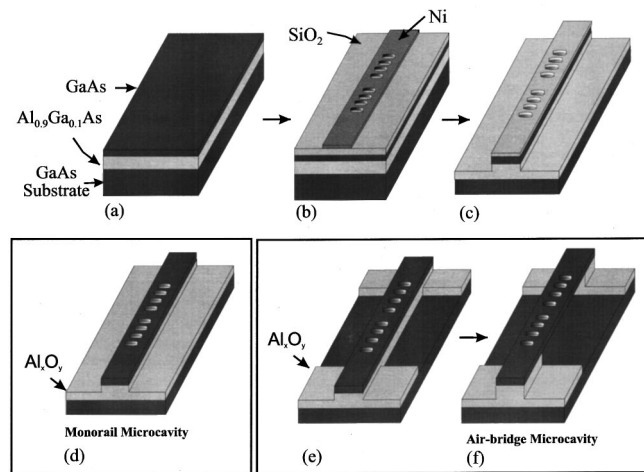

FIG. 2. Fabrication process of the one-dimensional PBG monorail and air-bridge microcavities. (a) Starting material. (b) After image reversal of patterns generated by direct-write electron-beam lithography. (c) After reactive ion etching of the $GaAs/Al_{0.93}Ga_{0.07}As$ heterostructure. (d) Completion of fabrication process for the monorail microcavity, after thermal oxidation of $Al_{0.93}Ga_{0.07}As$ material and facets cleavage. (e) After removal of trench material by reactive ion etching; trench pattern is defined by photolithography. (f) Completion of fabrication process for the air-bridge microcavity, after thermal oxidation of $Al_{0.93}Ga_{0.07}As$, photolithographic patterning of the trench area, sacrificial etch of Al_xO_y, and facets cleavage.

spective structure. For both the monorail and air-bridge microcavities, the transmission spectra are expected to exhibit band gaps extending from $\lambda = 1400$ to 1700 nm, with the resonant peaks located at and around 1550 nm. The transmission at the resonant wavelength is computed to be over 72% for the monorail and 90% for the air bridge, respectively. Input and output waveguides to and from the microcavities (not shown in Fig. 1) are also included to allow optical coupling into the microcavities during transmission measurement. To maximize the coupling of light into the devices, the waveguides are 3 μm wide at the input facets and narrow to the width of the microcavity structures over a distance of 100 μm. The overall length of the devices is 1.5 mm.

B. Device fabrication

A schematic depicting the fabrication process sequence is shown in Fig. 2. The heterostructures for both the monorail and air-bridge microcavities are deposited by gas-source molecular beam epitaxy [Fig. 2(a)]. The microcavity device design dictates that the GaAs waveguide be grown on a low refractive-index material of sufficient thickness to prevent optical loss through the substrate. The refractive index of Al_xO_y has been determined from prior transmission measurements of $GaAs/Al_xO_y$ distributed Bragg reflectors to be about 1.61. Simulations based on the beam propagation method indicate that an oxide thickness of at least 2 μm is, therefore, necessary for good mode confinement in the GaAs waveguide. Consequently, a target thickness of 2.5 μm for the high Al-composition $Al_xGa_{1-x}As$ layer is chosen for the growth process. The high Al composition is necessary for a reasonably fast oxidation rate and the addition of the small

amount of Ga in the alloy improves the stability of the oxide.[7] Using *ex situ* variable-angle spectroscopic ellipsometry, the final AlGaAs layer is measured to be 3.0 μm thick with an aluminum composition of 93%$\pm$1%. The GaAs layer thickness is similarly measured to be 185$\pm$1 nm for the monorail structure and 181$\pm$1 nm for the air-bridge structure. The GaAs and $Al_{0.93}Ga_{0.07}As$ layers are grown at temperatures of 600 and 670 °C, and at rates of 0.3 and 1.0 μm/h, respectively. Although the GaAs was undoped, the background carrier concentration is approximately 10^{16} cm^{-3} as measured by Hall effect measurements.

A layer of 100-nm-thick silicon dioxide (SiO_2) is next deposited on the GaAs/$Al_{0.93}Ga_{0.07}As$ heterostructure at 250 °C using plasma-enhanced chemical vapor deposition. The device patterns are then generated on a 200-nm-thick layer of the positive electron-beam resist polymethylmethacrylate (PMMA) using direct-write electron-beam lithography. Sixteen electron-beam exposure fields, approximately 100 μm$\times$100 μm in dimensions each, are stitched end to end to form the overall device structure of 1.5 mm in length. The exposed resist is developed in a 2:1 mixture of 2-propanol and methyl iso-butyl ketone at 20.0 °C for 90 s. A 30-nm-thick layer of nickel is next deposited on the sample by electron-beam evaporation. A subsequent lift-off of the nickel film results in the image reversal of the electron-beam written patterns [Fig. 2(b)]. Thereafter, the nickel film acts as a mask in the reactive ion etching (RIE) of the SiO_2 layer using a CHF_3/O_2 plasma. The process parameters are: CHF_3 flow rate of 50 sccm, O_2 flow rate of 5 sccm, process pressure of 50 mTorr, and incident rf power of 225 W, with an etch rate of about 100 nm/min. After the RIE process, the nickel mask is stripped off with a commercial etchant and the sample is backside-lapped down to approximately 150 μm.

A RIE process using $BCl_3/SiCl_4$ gases next transfers the device patterns on the SiO_2 mask into the GaAs/$Al_{0.93}Ga_{0.07}As$ heterostructure [Fig. 2(c)]. The process parameters are BCl_3 flow rate of 30 sccm, $SiCl_4$ flow rate of 20 sccm, process pressure of 30 mTorr, and incident rf power of 250 W. The RIE process, with an etch rate of approximately 220 nm/min, etches through the top GaAs layer and about 400 nm into the $Al_{0.93}Ga_{0.07}As$ layer. The process sequences for the monorail and the air-bridge microcavities diverge at this juncture. For the monorail microcavity, the SiO_2 mask layer is next removed by RIE and the sample introduced into an oxidation apparatus [Fig. 2(d)]. The apparatus consists of a single-zone furnace with a 2-in.-diam quartz tube. The sample in a quartz carrier is placed in the middle of the furnace tube during the oxidation process[8] and the furnace temperature is maintained at 435 °C. Steam is introduced into the furnace by flowing nitrogen through a water bubbler maintained at 90 °C. The nitrogen flow rate is approximately 2 l/min. An oxidation process that is 30 min in duration, as measured from the time when the sample has attained thermal equilibrium with the furnace and the steam is introduced, is sufficient to completely oxidize the $Al_{0.93}Ga_{0.07}As$
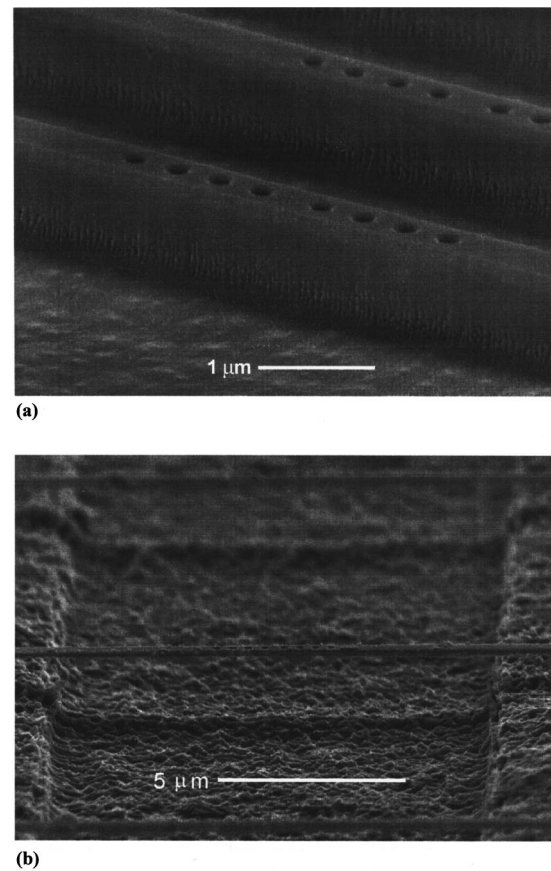

(a)

(b)

FIG. 3. Scanning electron micrographs of (a) the monorail microcavity and (b) the air-bridge microcavity.

remaining in the sample. This translates to a nominal oxidation rate of about 5 μm/h.

For the air-bridge microcavity, a photolithography step is next performed to define a 10-μm-wide trench pattern with the photonic crystal in the center of the trench. A RIE step then etches about 800 nm into the $Al_{0.93}Ga_{0.07}As$ material to define the trench region and remove the bulk of the sacrificial material. The resist and the SiO_2 mask are next removed using RIE [Fig. 2(e)]. Thereafter, the $Al_{0.93}Ga_{0.07}As$ layer is oxidized using the same apparatus and parameters as the monorail structure. Another photolithography step is performed to again define the same 10-μm-wide trench pattern. The sample is then dipped in a diluted hydrofluoric acid (HF) solution of 10 ml HF:250 ml deionized water that selectively etches the sacrificial oxide, hence, suspending the air-bridge structure [Fig. 2(f)]. The sample is immediately rinsed in a sequence of water, methanol, acetone, and methanol to both remove the resist and prevent the occurrence of stiction by virtue of the lower surface tension of methanol (as compared to water).

Finally, the facets to the input and output waveguides in both the monorail and air-bridge structures are cleaved to facilitate the coupling of light into the devices during optical characterization. Scanning electron micrographs of both the monorail and air-bridge microcavity structures are shown in Figs. 3(a) and 3(b), respectively.

Monorail Microcavities
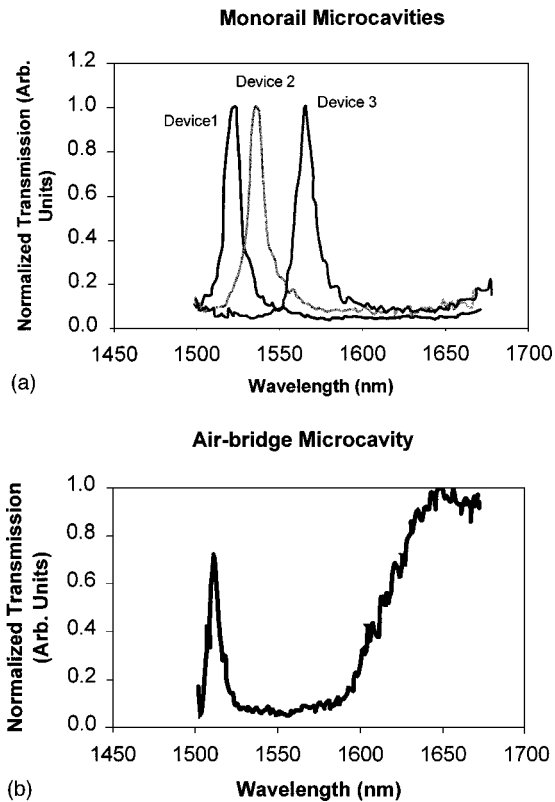

(a)

Air-bridge Microcavity

(b)

FIG. 4. Normalized transmission spectra of (a) monorail microcavities and (b) an air-bridge microcavity. In (a), the resonant transmission peaks correspond to three microcavities with different defect sizes. The band edges are outside the wavelength range of the measurement setup. In (b), both the resonant transmission peak and the upper band edge are visible.

III. OPTICAL CHARACTERIZATION

Optical transmission measurements of the devices are performed with a continuous-wave NaCl:OH$^-$ color-center laser that is tunable from 1500 to 1670 nm and has an output power of 250 mW at the center of its gain curve. The laser output is coupled through an optical fiber and into an input waveguide of a device with a fiber lens assembly. A $10\times$ microscope objective collects the light from the output facet and images the output onto a photodetector through a pinhole. An additional photodetector monitors the input power, and a computer calculates the ratio of the output and input powers to generate a relative transmission spectrum.

Figures 4(a) and 4(b) show the respective transmission spectra of the monorail and air-bridge microcavities within the range of measurement. Note that the wavelength range accessible with the measurement setup is narrower than the width of the stop band, and encompasses only the resonance peak and at most one of the stop-band edges. The cavity quality factor Q of the resonance is defined as $\lambda_{res}/\Delta\lambda$, where λ_{res} is the resonant wavelength and $\Delta\lambda$ is the full width at half maximum of the resonance peak. For the monorail microcavities, the resonance peaks are located at 1522 nm [device 1 in Fig. 4(a)], 1536 nm (device 2), and 1566 nm

(device 3), corresponding to 5% increments in defect sizes between devices from device 1 to 3. An increase in the defect size clearly results in the shift of the resonance peak to a longer wavelength. The resonances have Q's of 136, 142, and 117, respectively. The air-bridge microcavity has a resonance at 1525 nm with a higher Q of 230. The long-wavelength edge of the photonic band gap is also visible for this particular air-bridge microcavity. The resonant modal volumes associated with these microcavities are about 0.056 μm^3, implying one of the highest Q/V ratios that has ever been measured.[9] This work also represents the first measurement at optical wavelengths of PBG microcavities realized with a direct-band-gap semiconductor.

It is worthy to note that the tunability of the resonant wavelength by changing the defect dimensions also reflects the sensitivity of such high-index contrast systems to deviation in device dimensions. Consequently, stringent demand is placed on the nanoscale-dimensional control of the fabrication process to achieve predictability in device performance.

IV. CONCLUSION

One-dimensional photonic band-gap waveguide microcavities have been successfully fabricated using III–V compound semiconductors and optically characterized at the optical communication wavelength regime of 1550 nm. The use of direct-band-gap semiconductors in this effort suggests the deployment of the PBG microcavities in active device applications. These microcavities may constitute an important component in the implementation of low-threshold semiconductor nanolasers and the monolithic integration optoelectronic devices.

ACKNOWLEDGMENTS

[1] D. Kleppner, Phys. Rev. Lett. **47**, 233 (1981).
[2] H. Yokoyama and S. D. Brorson, J. Appl. Phys. **66**, 4801 (1989).
[3] E. Yablonovitch, Phys. Rev. Lett. **58**, 2059 (1987).
[4] J. D. Joannopoulos, P. R. Villeneuve, and S. Fan, Nature (London) **386**, 143 (1997).
[5] P. R. Villeneuve, S. Fan, J. D. Joannopoulos, K.-Y. Lim, G. S. Petrich, L. A. Kolodziejski, and R. Reif, Appl. Phys. Lett. **67**, 167 (1995).
[6] P. R. Villeneuve, S. Fan, J. D. Joannopoulos, K.-Y. Lim, J. C. Chen, G. S. Petrich, L. A. Kolodziejski, and R. Reif, in *Proceedings of NATO Advanced Studies Institute on Photonic Band Gap Materials, Elounde, Greece, 1995* (Kluwer, Dordrecht, 1995), p. 411.
[7] K. D. Choquette, K. M. Geib, R. Hull, H. Q. Hou, K. L. Lear, H. C. Chui, B. E. Hammons, and J. A. Nevers, *Proceedings of the 1996 IEEE LEOS Annual Meeting* (IEEE, Piscataway, NJ, 1996), p. 390.
[8] J. M. Dallesasse, N. Holonyak, Jr., A. R. Sugg, T. A. Richard, and N. El-Zein, Appl. Phys. Lett. **57**, 2844 (1990).
[9] J. S. Foresi, P. R. Villeneuve, J. Ferrera, E. R. Thoen, G. Steinmeyer, S. Fan, J. D. Joannopoulos, L. C. Kimerling, H. I. Smith, and E. P. Ippen, Nature (London) **390**, 143 (1997).